arXiv:2110.01601v2 [cs.LG] 13 Oct 2021

NeuFENet: Neural Finite Element Solutions with Theoretical Bounds for Parametric PDEs

Biswajit Khara[1], Aditya Balu[1], Ameya Joshi[2], Soumik Sarkar[1], Chinmay Hegde[2], Adarsh Krishnamurthy[1], Baskar Ganapathysubramanian[1]*

[1] Iowa State University
[2] New York University
* Corresponding author: barkarg@iastate.edu

Abstract

We consider a mesh-based approach for training a neural network to produce field predictions of solutions to parametric partial differential equations (PDEs). This approach contrasts current approaches for "neural PDE solvers" that employ collocation-based methods to make point-wise predictions of solutions to PDEs. This approach has the advantage of naturally enforcing different boundary conditions as well as ease of invoking well-developed PDE theory–including analysis of numerical stability and convergence– to obtain capacity bounds for our proposed neural networks in discretized domains. We explore our mesh-based strategy, called NeuFENet, using a weighted Galerkin loss function based on the Finite Element Method (FEM) on a parametric elliptic PDE. The weighted Galerkin loss (FEM loss) is similar to an energy functional that produces improved solutions, satisfies *a priori* mesh convergence, and can model Dirichlet and Neumann boundary conditions. We prove theoretically, and illustrate with experiments, convergence results analogous to mesh convergence analysis deployed in finite element solutions to PDEs. These results suggest that a mesh-based neural network approach serves as a promising approach for solving parametric PDEs with theoretical bounds.

Keywords

Neural solvers | Deep learning | Physics informed learning | Parametric PDE | Data-free modeling

1 Introduction

Scientific machine learning is an emerging field that combines developments in machine learning with scientific computation methods. This field has witnessed a variety of approaches that deploy neural networks to solve partial differential equations (PDE). Such *neural PDE solvers* provide a very different strategy of solving differential equations as compared to the traditional numerical methods; they primarily rely on *optimization* techniques rather than the exact solution of systems of equations. This recent explosion in this line of work was initiated by the seminal paper on Physics Informed Neural Networks (PINNs) [1].

In terms of the amount of data usage, neural PDE solvers span a wide spectrum. Some methods are "data-driven" [2–5], where the solution to a given PDE is constructed from available experimental data or the underlying PDE is inferred from available data (commonly termed as the discovery of hidden physics). In contrast, at the other end of the spectrum are the so-called "data-free" methods that do not rely on input-output pairs but solely use the PDE and the boundary conditions to obtain the solution. In the past few years, many such methods have been proposed [5–15]. Our work in this paper follows the latter data-free approach.

The core of neural PDE solvers are deep neural networks, which can represent arbitrarily complicated functions from the input to the output domain and, therefore, can approximate the PDE solution. Most neural methods use a pointwise prediction framework (also known as implicit neural networks [16]). These pointwise prediction frameworks take $\mathbf{x} \in D$ (the spatial coordinates of the field) as input and produce an output solution value of $u(\mathbf{x})$ (the solution field value at $\mathbf{x}$) as shown in Figure 1a. Thus, the neural PDE solvers create a mapping between the input domain D to the range of the solution. Due to a pointwise prediction framework, these methods do not require a mesh and thus rely on collocating points from the domain. To take advantage of the modern stochastic gradient descent (SGD) based methods, this set of collocation points are often selected in a random or quasi-random manner [17]. The trained network approximates the discrete solution via a complicated and nonlinear mapping. This is in contrast to classical numerical PDE approaches which usually rely on a linear combination of local functions with limited differentiability (even when the exact solution may be analytic). However, such poinwise prediction neural methods do not naturally account for the domain topology. In particular, the "local" nature of the solution and sparsity of matrices that emerges naturally in classical methods are missing in these neural methods. Some researchers have explored the idea of using classical methods such as finite difference methods (FDM) and finite volume methods (FVM) to construct neural architectures for solving PDEs [18–20].

Inspired by traditional numerical techniques, these frameworks construct a mapping between an input field and the solution field while using the discretization techniques associated with conventional numerical methods. These methods take advantage of the "local" nature of the solution and sparsity of matrices, similar to traditional numerical methods. In particular, mathematical concepts from finite element methods (FEM) are naturally translatable to neural networks (quadrature can be represented as convolutions), and provide interesting possibilities including variational arguments (monotone convergence to the solution), mesh convergence, basis order based convergence, and natural incorporation of boundary conditions. The current work builds upon these ideas.

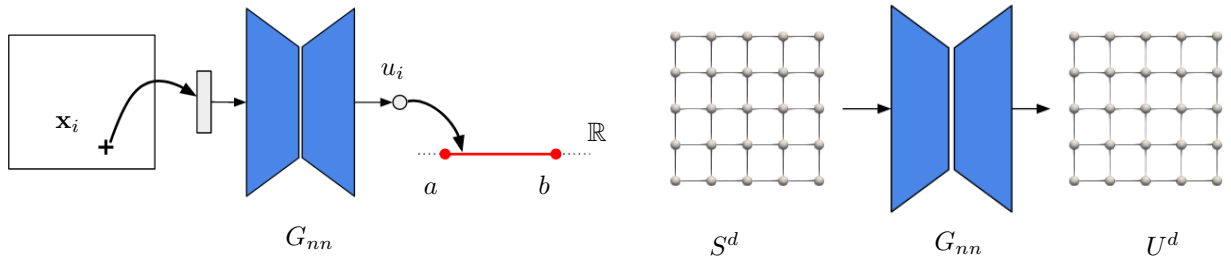
Neural architecture: In this paper, we develop a finite element (FEM) based neural architecture for solving PDEs. Figure 1b shows an abstract outline of this idea where the mapping is obtained with the use of convolutional neural networks, a specific class of network architectures specialized in learning from discrete domains such as input field S^d and the output field U^d as shown in Figure 1b. The nature of the input field S^d and the output field U^d (in Figure 1b) would depend on the actual PDE under consideration and will be made more concrete in later sections. To the best of the knowledge of the authors, no efforts have been made to develop FEM-based neural architectures. There are several benefits in developing a finite element method (FEM) based neural architecture. FEM based numerical methods are often backed by a well developed and elegant theory that connects the discretization of the domain (in terms of element/cell dimension, h) and the properties of the basis functions used to approximate the field (in terms of polynomial order, α) with the quality of the ensuing numerical solution to the PDE. In particular, numerical stability arguments and *a priori* error estimates allow users to judiciously reason about the accuracy, robustness, and convergence [21, 22]. Such theoretical arguments rely on the spatial discretization of the domain and properties of the basis functions in finite elements[1].

Loss functions: Having decided on borrowing the discretization scheme from FEM, there are multiple avenues to define the loss function. First, we need to define the spatial derivatives at each quadrature point. In FEM, this is done by directly differentiating the basis functions. Pointwise prediction methods perform this by differentiating the neural network with respect to the input variable. The differentiation process in the numerical method is straightforward and interpretable, while that is not necessarily the case in pointwise neural methods. Once the spatial derivatives are defined via the basis functions, we can either compare the weak form against the predefined basis functions from the test function space and perform a residual minimization or use an energy minimization approach. In the present work, we choose the latter, also known as the Rayleigh-Ritz (RR) method [26, 27]. The RR method states that the solution to a PDE must be the stationary point of some functional (i.e., "energy") under certain conditions. We note that the RR method has been used in a neural network for solving PDEs before [28]. However, the approach used there closely matches the pointwise prediction approach outlined in Figure 1a, in contrast to our proposed approach.

Boundary conditions: The imposition of boundary conditions can also be challenging in neural methods. Very few neural methods satisfy/apply the boundary conditions exactly [29–32], with most methods relying on approximate approaches [1, 7, 33] usually by including an additional loss function corresponding to the imposed boundary conditions. It has been shown by Van der Meer et al. [34] and Wang et al. [35] that these losses have to be carefully weighed, making this a non-trivial exercise in hyperparameter tuning. This hyperparameter sensitivity underlines the difficulty of applying the boundary conditions in a neural network-based method (or simply neural method). Also, note that the method in [28] (using RR method) is unable to apply the Dirichlet boundary conditions precisely and consequently make use of a penalty-based approach for imposing a Dirichlet boundary condition, which we avoid altogether.

Parametric PDEs: Going beyond a single PDEs, there is growing interest in neural approaches that solve parametric PDEs (i.e., PDEs defined by a family of parametrized boundary conditions or coefficient fields). Most neural PDE methods have so far been limited to solving for a single instance of the PDE than a class of parametric solutions. Extending a instance PDE solver into a parametric PDE solver can greatly augment rapid design exploration, as alluded to in SimNet [36] and Wang and Perdikaris [37], where the authors build a conventional implicit neural solver for parametric PDEs.

[1] In contrast, state-of-art neural methods allow us to use basis functions beyond polynomials/Fourier bases and approximate much more complicated mappings. Although such methods *can* be analyzed theoretically, the estimates are often impractical [23–25]. This is a very active area of research, and we expect tighter estimates in the near future.



(a) *Conventional neural view: domain-to-range mapping*

(b) *A more complex view: field-to-field mapping*

Figure 1: *(a) Several neural methods (like [1, 30]) are trained to produce point predictions: $G_{nn} : D \to \mathbb{R}$, which are easier to train, but more difficult to analyze and converge [39, 40], (b) In the* NEUFENET *approach, we train a neural network to produce a discretized field solution over a mesh. Such an approach directly links powerful PDE analysis techniques at the cost of a larger network. The terms S^d and U^d can be considered the discrete version of any meaningful pair of input and output relevant to the PDE; these will be made precise in the next section.*

In this paper, we build upon recent efforts that train networks to predict the full-field solution [15, 18, 38] on parametric PDEs. Our contributions are as follows:

1. We present an algorithm that bridges traditional numerical methods with neural methods. The neural network is designed to map inputs to the discretized field solution u. However, the neural network is *not responsible* for ensuring the spatial differentiability of the solution. Rather, the discrete field solution relies on traditional numerical methods (and associated numerical differentiation and quadrature) to construct the loss function. Such an approach allows the natural incorporation of different boundary conditions and allows *a priori* error estimates.
2. We define the loss functions based on the Rayleigh-Ritz method coupled with the approximation scheme provided by a continuous Galerkin FEM. By defining such loss functions, we utilize function spaces with appropriate differentiability. This also account for the "local" nature of the solution resulting in computationally efficient loss evaluations.
3. We prove error convergence (similar to conventional mesh convergence) for a particular class of PDEs.
4. We demonstrate NEUFENET's performance on linear Poisson equation in 2D and 3D with both Dirichlet and Neumann boundary conditions. Further, we test the parametric capability of this method on Poisson's equation, by considering a case involving stochastic diffusivity which requires access to a parameteric PDE solver.

The rest of the paper is arranged as follows: the definitions and terminologies regarding the parametric Poisson's equation are introduced in Section 2 and the mathematical formulations are described in detail in Section 3. The implementation aspects of NEUFENET are described in Section 4. Section 5 presents a theoretical analysis of the errors and finally computational results are presented in Section 6.

2 Mathematical Preliminaries

Consider a bounded open (spatial) domain $D \in \mathbb{R}^n, n \geq 2$ with a Lipschitz continuous boundary $\Gamma = \partial D$. We will denote the domain variable as $\mathbf{x}$, where the boldface denotes a vector or tuple of real numbers. In $\mathbb{R}^n$, we have $\mathbf{x} = (x_1, x_2, \ldots, x_n)$; but for 2D and 3D domains, we will frequently use the notation $\mathbf{x} = (x, y)$ and $\mathbf{x} = (x, y, z)$ respectively. Consider also a probability space (Ω, F, P), where Ω is the sample space, F is the σ-algebra of the subsets of Ω and P, a probability measure. We consider an abstract PDE on the function $u : D \times \Omega \to \mathbb{R}$ as:

$$\mathcal{N}[u; s(\mathbf{x}, \omega)] = f(\mathbf{x}), \quad \mathbf{x} \in D,\ \omega \in \Omega \tag{1a}$$

$$\mathcal{B}[u] = g(\mathbf{x}), \quad \mathbf{x} \in \Gamma. \tag{1b}$$

Here, $\mathcal{N}$ is a differential operator (possibly nonlinear) operating on a function u. The differential equation depends on the input-data (e.g., material property) s which in turn is a function of the domain variable $\mathbf{x}$ and parameter $\omega \in \Omega$. Thus $\mathcal{N}$ is essentially a family of PDE's parameterized by ω. [2] $\mathcal{B}$ is a boundary operator on u. In general, there can be multiple boundary operators for different part of the boundary Γ.

[2] While a probability based definition of ω is not needed for defining a parameteric PDE, we choose this definition for two reasons. First, such a formulation allows easy extension to the stochastic PDE case. Second, such a formulation will allow using expectation based arguments in the analysis of convergence.

Given a PDE along with some boundary conditions, such as the one presented in Equation 1, the goal is to find a solution u that satisfies Equation 1 as accurately as possible. Previous works such as [1, 7, 30] seek to find a pointwise mapping $u : D \to \mathbb{R}$. Here (see next section), by coupling deep neural networks with numerical methods, we explore other mappings to retrieve a discrete field solution.

In this work, we focus on the Poisson's equation considering both Dirichlet and Neumann boundary conditions, along with a heterogeneous and stochastic diffusivity:

$$-\nabla \cdot (\nu(\mathbf{x}, \omega)\nabla u) = f(\mathbf{x}) \text{ in } D \tag{2}$$

along with the boundary conditions

$$u = g \text{ on } \Gamma_D \tag{3}$$

$$\frac{\partial u}{\partial n} = h \text{ on } \Gamma_N \tag{4}$$

where ν is the *permeability* (or *diffusivity*) which depends on both $\mathbf{x}$ and the random variable ω; and f is the forcing. In relation to Equation 1, ν plays the role of the data s. Γ_D and Γ_N are the boundaries of the domain D where Dirichlet and Neumann conditions are specified respectively. We will assume that $\partial D = \Gamma = \Gamma_D \cup \Gamma_N$.

2.1 Poisson's equation in heterogeneous media

We are mostly interested in the problem of a steady state mass (or heat) transfer through an inhomogeneous medium (material). This essentially means that the material has different properties at different points. The only material property appearing in the Poisson's equation (Equation 2) is $\nu(\mathbf{x})$, thus the inhomogeneity can be modeled by a spatially varying ν, i.e., $\nu = \nu(\mathbf{x})$. The equation and the BC's are given by:

$$-\nabla \cdot (\tilde{\nu}(\mathbf{x})\nabla u) = 0 \text{ in } D \tag{5a}$$

$$u(0, y) = 1 \tag{5b}$$

$$u(1, y) = 0 \tag{5c}$$

$$\frac{\partial u}{\partial y}(x, 0) = 0 \tag{5d}$$

$$\frac{\partial u}{\partial y}(x, 1) = 0 \tag{5e}$$

where D is a hypercube domain in $\mathbb{R}^n$, $n = 2, 3$. The diffusivity/permeability $\tilde{\nu}$ is heterogeneous with respect to $\mathbf{x}$ and is also parameterized by $\omega \in \Omega$. The specific form of $\tilde{\nu}$ is given in Equation 47.

3 Formulations

3.1 Neural approximation of the solution

Instead of seeking a mapping between the domain and an interval on the real line (Figure 1(a)), we seek a mapping between the input s and the full field solution u in the discrete spaces (Figure 1(b)). S^d denotes the discrete representation of the known quantity s. S^d could be either available only at discrete points (perhaps from some experimental data); or in many cases, s might be known in a functional form and thus S^d will be simply the values of s evaluated on the discrete points. Therefore, if we denote a NEUFENET (see Figure 1(b)) network by G_{nn}, then G_{nn} takes as input a discrete or functional representation of s and outputs a discrete solution field U^d_θ as:

$$U^d_\theta = G_{nn}(S^d; \theta), \tag{6}$$

where θ denote the network parameters. The mathematical formulations presented in this section only assumes a suitable neural network that provides the aforementioned mapping between S^d and U^d. The actual network architecture is discussed in Section 4.1.

An untrained network, as expected, will produce a mapping that does not satisfy the discrete PDE and will possess a large error. Our goal is to bring this error down to an acceptable level, and thereby reaching a solution that is "close enough" to the exact solution. We do this by designing the loss function based on major ideas taken from the classical numerical methods, as explained below.

3.2 Loss functions inspired by variational methods

The design of the loss function, along with the choice of the neural mapping, forms the central part of our approach. The finite element based loss function is inspired by the Galerkin formulation of an elliptic PDE as well as the Rayleigh-Ritz method. In this case, we actually construct a function of certain regularity in the domain variable $\mathbf{x}$, as opposed to just assuming a function of certain differentiability at the collocation points.

Suppose $H^1(D) = W^{1,2}(D)$ denotes the Sobolev space of functions whose first derivatives are square integrable. Define the space V as

$$V = \left\{ v \in H^1(D) : v(0, y) = 1, v(1, y) = 0, \|v\|_V < \infty \right\}, \tag{7}$$

where $\|v\|_V$ is defined as:

$$\|v\|_V = \int_D \nu(\mathbf{x}) |\nabla v|^2 d\mathbf{x}. \tag{8}$$

Then the Galerkin formulation for the Poisson's equation presented in Equation 5 is to find $u \in V$ such that,

$$B(u, w) = L(w) \;\; \forall w \in V, \tag{9}$$

where,

$$B(u, w) = \int_D \nu(\nabla w \cdot \nabla u) d\mathbf{x} \tag{10a}$$

$$L(w) = \int_D w f d\mathbf{x}. \tag{10b}$$

Equation 9 actually represents a number of equations each for a different test function w taken from the space V. Thus, if V is discretized such that it can be represented by a finite basis, then the Galerkin formulation (Equation 9) yields a finite system of algebraic equations.

From the theory of variational calculus [26, 41], it is also known that Equation 9 is the Euler-Lagrange equation of the following functional $J(u)$ of $u \in V$:

$$J(u) = \frac{1}{2} B(u, u) - L(u). \tag{11}$$

Therefore, the solution u can also be written as the minimizer of the cost function J:

$$u = \arg\min_{u \in V} J(u). \tag{12}$$

In NEUFENET, we make use of this functional J, but instead of minimizing it against the solution u, we minimize it against the network parameters θ. Since V is an infinite dimensional space, we need to discretize it to a finite subspace where we can evaluate J. For this, let $\mathcal{K}^h$ be a discretization of D into n_{el} finite elements K_i such that $\cup_{n_{el}} K_i = D$. Then the discrete function space V^h is define as:

$$V^h = \left\{ v^h \in V : v^h|_K \in P_m(K), \; K \in \mathcal{K}^h \right\}, \tag{13}$$

where $P_m(K)$ denotes the set of polynomial functions of degree m define on K. Let the dimension of V^h be N, which essentially means that the number of unknowns in the domain is also N. Suppose $\{\phi_i(\mathbf{x})\}_{i=1}^N$ is a suitable basis that span V^h. Then any function $u^h \in V^h$ can be written as

$$u^h(\mathbf{x}) = \sum_{i=1}^{N} \phi_i(\mathbf{x}) U_i, \tag{14}$$

where U_i are the function values at the nodal points in the mesh $\mathcal{K}^h$. Then Equation 12 can be rewritten for u^h as:

$$u^h = \arg\min_{u^h \in V^h} J(u^h). \tag{15}$$

This minimization of the energy functional in a finite dimensional space is commonly known as the Rayleigh-Ritz method. But in the presence of a neural network, we minimize J with respect to the network parameter θ instead of u^h. For this, we need to first explicitly state the θ dependence of u^h. This can be done by a slight modification to Equation 14 as below:

$$u^h(\mathbf{x};\theta) = \sum_{i=1}^{N} \phi_i(\mathbf{x}) U_i(\theta), \tag{16}$$

along with a generalization of the function space V^h as:

$$V_\theta^{h'} = \left\{ v(\theta) \in V^h : v(x=0,y;\theta) = 1, v(x=1,y;\theta) = 0 \right\}. \tag{17}$$

Then we can finally write down the NEUFENET solution $u^h_{\theta^*}$ in two steps:

$$\theta^* = \arg\min_{\theta\in\Theta} J(u^h(\mathbf{x};\theta)) \tag{18a}$$

$$u^h_{\theta^*} = u^h(\mathbf{x};\theta^*), \tag{18b}$$

where $u^h_{\theta^*} \in V_\theta^{h'}$.

The discussion leading to Equation 18 is based on a non-parametric diffusivity, i.e., $\tilde{\nu} = \nu(\mathbf{x})$. Extension of this formulation to the parametric PDE case is straightforward. Specifically, for a parameterized ω, i.e., $\tilde{\nu} = \nu(\mathbf{x},\omega)$, the function space $V_\theta^{h'}$ is modified as:

$$V_\theta^h = \left\{ v : \|v(\mathbf{x},\omega;\theta)\|_{V_\theta^h} < \infty,\ v(x=0,y,\omega;\theta) = 1, v(x=1,y,\omega;\theta) = 0 \right\} \tag{19}$$

where, $\|\cdot\|_{V_\theta^h}$ is the energy norm

$$\|v\|^2_{V_\theta^h} = \mathbb{E}_{\omega\sim\Omega}\left[\int_D \nu(\mathbf{x},\omega;\theta) |\nabla v|^2 d\mathbf{x} \right]. \tag{20}$$

With this choice of function space, the NEUFENET loss function can be written as:

$$L_{\text{NEUFENET}}(\theta) = \mathbb{E}_{\omega\in\Omega} J(u^h(\mathbf{x},\omega;\theta)) \tag{21}$$

The right hand side of Equation 21 involves two integrations: one over the spatial domain D and the other an expectation over Ω. The integration over D is evaluated numerically using Gaussian quadratures rules. And the expectation over Ω is evaluated approximately by a summation over a finite number of samples, i.e.,

$$\hat{L}_{\text{NEUFENET}}(\theta) = \frac{1}{N_s} \sum_{i=1}^{N_s} J(s(\omega_i), u^h(\mathbf{x},\omega_i);\theta). \tag{22}$$

The loss function $\hat{L}_{\text{NEUFENET}}(\theta)$ is now just a function of θ and we can minimize it with respect to θ,

$$\theta^* = \arg\min_{\theta\in\Theta} \hat{L}_{\text{NEUFENET}}(\theta) \tag{23a}$$

$$u^h_{\theta^*} = u^h(\mathbf{x},\omega;\theta^*). \tag{23b}$$

Remark 1. To simplify notations when we analyze errors in Section 5, we make a distinction between two representations of θ^*: one of them is the theoretical minimum (denoted by $\tilde{\theta}$ in Section 5) and the other is the *actual* set of parameters (denoted by θ in Section 5) obtained by optimizing Equation 23a with an optimization algorithm. This terminology then spawns two variants for $u^h_{\theta^*}$: $u_{\tilde{\theta}}$ and u_θ respectively.

Algorithm 1 Algorithm for instance PDE solver

Require: S^d, α, TOL and `max_epoch` ▷ α = learning rate

Initialize G_{nn}
for `epoch` $\leftarrow$ 1 to `max_epoch` **do**
  $U_\theta^d \leftarrow G_{nn}(S^d)$
  Apply Dirichlet boundary conditions to U_θ^d
  $loss = L_{\text{NEUFENET}}(S^d, U_\theta^d)$
  $\theta \leftarrow optimizer(\theta, \alpha, \nabla_\theta(loss))$
  if $loss <$ TOL **then**
    `break`
  end if
end for

Algorithm 2 Algorithm for parametric PDE solver

Require: $\{S_i^d\}_{i=1}^{N_s}$, α, TOL and `max_epoch` ▷ α = learning rate

Initialize G_{nn}
for `epoch` $\leftarrow$ 1 to `max_epoch` **do**
  for `mb` $\leftarrow$ 1 to `max_mini_batches` **do**
    Sample $(S^d)_{mb}$ from the set $\{S_i^d\}_{i=1}^{N_s}$
    $(U_\theta^d)_{mb} \leftarrow G_{nn}\Big((S^d)_{mb}\Big)$
    Apply Dirichlet boundary conditions on $(U_\theta^d)_{mb}$
    $loss_{mb} = L_{\text{NEUFENET}}((S_\theta^d)_{mb}, (U_\theta^d)_{mb})$
    $\theta \leftarrow optimizer(\theta, \alpha, \nabla_\theta(loss_{mb}))$
  end for
end for

3.3 Training algorithm for NEUFENET

We provide two versions of the training algorithm. (i) an algorithm for computing the solution for an instance of a PDE and (ii) an algorithm for approximating the solution for a parametric PDE. The model architecture and the loss function remain the same for both. For the instance version, we use a simple approach as explained in Algorithm 1. While sampling from a distribution of coefficients/forcing field for a parametric PDE, we employ the mini-batch based optimization approach as explained in Algorithm 2. The sampling of the known quantities can be performed by using any random or qseudo-random sequence (see Section 6.2 for an example). For training the neural network, we predict the solution field using sampled inputs and compute the loss using the loss function derived above. We employ gradient descent based optimizers such as Adam [42] to perform the numerical optimization.

4 Implementations

4.1 Model architecture for NEUFENET

Due to the structured grid representation of $\mathcal{S}^d$ and similar structured representation of U_θ^d, deep convolutional neural networks are a natural choice of network architecture. The spatial localization of convolutional neural networks helps in learning the interaction between the discrete points locally. Since the network takes an input of a discrete grid representation (similar to an image, possibly with multiple channels) and predicts an output of the solution field of a discrete grid representation (similar to an image, possibly with multiple channels), this is considered to be similar to an image segmentation or image-to-image translation task in computer vision. U-Nets [43, 44] have been known to be effective for applications such as semantic segmentation and image reconstruction. Due to its success in diverse applications, we choose U-Net architecture for NEUFENET. The architecture of the network is shown in Figure 4. First, a block of convolution, and instance normalization is applied. Then, the output is saved for later use via skip-connection. This intermediate output is then down sampled to a lower resolution for a subsequent block of convolution, instance normalization layers. This process is continued for two more times. Now, the upsampling starts where, the saved outputs of similar dimensions are concatenated with the output of upsampling for creating the skip-connections followed by a convolution layer. LeakyReLU activation was used for all the intermediate layers. The final layer has a Sigmoid

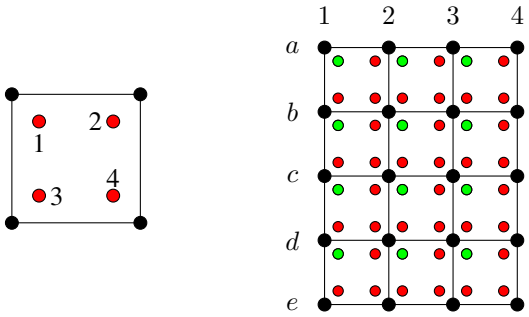


Figure 2: *(Left) A single 2D element in FEM, with black dots denoting "nodes" and red dots denoting 2×2 Gauss quadrature points. (Right) A finite element mesh, with 4×3 linear elements and 5×4 nodes. Each of these elements contains Gauss points for integration to be performed within that element. Within each element, the "first" quadrature point (marked "1" on left) is marked green, and others red.*

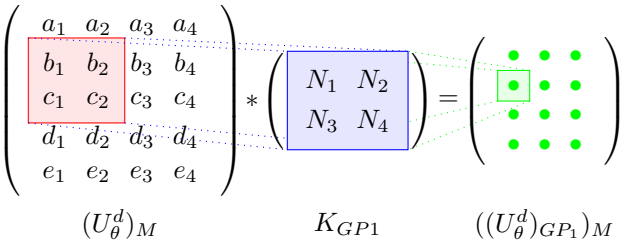


Figure 3: *Quadrature quantity evaluation in FEM context. $(U_\theta^d)_M$ is the matrix view of the nodal values. K_{GP1} is kernel containing the basis function values at "gauss point - 1" (top left corner). This convolution results in the function values evaluated at the Gauss point "1" of each element (marked green). $(U_\theta^d{}_{GP1})_M$ is the matrix of this result. Function values (or their derivatives) evaluated at Gauss points can then be used in any integral evaluation. For example, $\int u^h dD = |J| \sum_{I \in M} \left[\sum_{i=1}^{4} (w_i (U_\theta^d)_{GPi})_M \right]$, where $|J|$ is the transformation Jacobian for integration and w are the quadrature weights.*

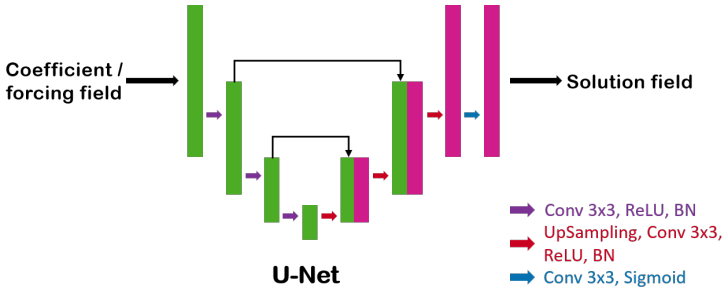


Figure 4: *UNet architecture used for training* NEUFENET.

activation.

4.2 Applying boundary conditions

In NEUFENET, the Dirichlet boundary conditions are applied exactly. The output U_θ^d does not contain the boundary conditions. Thus, a small post-processing step is done to the network output to force the Dirichlet boundary conditions onto the respective boundaries. This can be done in a differentiable manner in modern machine learning software libraries such as PyTorch [45]. This exact imposition of Dirichlet boundary conditions allow the training process to be much smoother and interpretable, because there is no penalty term involved in the loss function. Thus the loss function retains its convex nature with respect to the solution u^h.

On the other hand, Neumann conditions are included in the variational form of the PDE right at the continuous level. Especially zero-Neumann conditions are exactly satisfied at the discrete level without requiring us to do anything ("do-nothing" conditions).

4.3 Calculation of derivatives and integration

The full domain integration (i.e., $\int D$) is nothing but the simple sum of the integration over the individual elements (i.e., $\sum_{i=1}^{N_{el}} \int D_i$). This integration over an individual element is in turn the simple weighted sum of the integrand evaluated at the Gauss quadrature points. This evaluation at a single Gauss point can be represented as convolution. Thus, if there are 4 Gauss points in each element, then 4 convolution operations will evaluate the integrand at those points for each element. After that, we only need to sum across Gauss points first, then followed by a sum across elements. See Figure 2 and Figure 3 for visualized representation of this process.

Remark 2. Since the result of the integration process is a scalar loss value, there is no requirement to compute, store or assemble a matrix.

5 Error analysis

5.1 Error analysis for the instance case

We provide estimates on the errors incurred by NEUFENET in approximating the solution. Suppose the exact solution of Equation 5 is u and the solution obtained at the end of the training process is given by u_θ (see Remark 1). Let us also define $u_{\tilde{\theta}}$ as the best possible function in V_θ. Note that this function may or may not be able to match u^h, but it represents the best possible function that the neural network function class can produce. Note also that $u_{\tilde{\theta}}$ might be different than u_θ, especially if the optimization algorithm is not able to reach the optimum $\tilde{\theta}$. We try to bound the error $u_\theta - u$ by first breaking down the total error into errors from different sources. Theorem 5.6 is our main result for the single instance PDE version, while Thoerem 5.8 is our main reuslt for the parametric PDE version.

Lemma 5.1. *Let u_θ be the solution of Equation 11 when it is optimized by Algorithm 1. Then the optimization error $\|e_\theta\|_{V^h} = \sqrt{2\|\mathcal{E}_J\|_1}$, where $e_\theta = u_\theta - u_{\tilde{\theta}}$ and $\mathcal{E}_J = J(u_\theta) - J(u_{\tilde{\theta}})$.*

Proof.

$$
\begin{aligned}
J(u_\theta) &= \int_D \left[\frac{1}{2}\nu|\nabla u_\theta|^2 - f u_\theta\right] d\mathbf{x} \\
&= \int_D \left[\frac{1}{2}\nu|\nabla u_{\tilde{\theta}} + \nabla e_\theta|^2 - f(u_{\tilde{\theta}} + e_\theta)\right] d\mathbf{x} \;\; (\text{using } e_\theta = u_\theta - u_{\tilde{\theta}}) \\
&= \int_D \left[\frac{1}{2}\nu|\nabla u_{\tilde{\theta}}|^2 + \frac{1}{2}\nu|\nabla e_\theta|^2 + \nu\nabla u_{\tilde{\theta}} \cdot \nabla e_\theta - f(u_{\tilde{\theta}} + e_\theta)\right] d\mathbf{x} \\
&= \int_D \left[\frac{1}{2}\nu|\nabla u_{\tilde{\theta}}|^2 - f u_{\tilde{\theta}}\right] d\mathbf{x} + \frac{1}{2}\int_D \nu|\nabla e_\theta|^2 d\mathbf{x} + \int_D \left[\nu\nabla e_\theta \cdot \nabla u_{\tilde{\theta}} - f e_\theta\right] d\mathbf{x} \\
&= J(u_{\tilde{\theta}}) + \frac{1}{2}\|e_\theta\|^2_{V^h}
\end{aligned}
\tag{24}
$$

where in the final step, we have used the definitions of J and $\|e_\theta\|_{V^h}$ along with the fact that $\int_D \left[\nu\nabla e_\theta \cdot \nabla u_{\tilde{\theta}} - f e_\theta\right] d\mathbf{x} = 0$ since $e_\theta \in V^h$ (see Equation 9 and Equation 10). Therefore, we have

$$
\|e_\theta\|^2_{V^h} = 2\left[J(u_\theta) - J(u_{\tilde{\theta}})\right] = 2\mathcal{E}_J = 2\|\mathcal{E}_J\|_1, \tag{25}
$$

since $\mathcal{E}_J = J(u_\theta) - J(u_{\tilde{\theta}}) > 0$. ■

We next describe a theorem that provides an estimate on the network capacity.

Theorem 5.2. *Fix $p \in \Omega$ and consider a PDE as defined in Equation 1 over a compact domain D which is uniformly discretized with resolution h. Let u_h^* be the true solution evaluated at the grid points. Consider the hypothesis class:*

$$
\mathcal{H} := \{u_\Theta : p \mapsto \sum_{l=1}^{k} a_l^i ReLU(\langle w_l^i, p\rangle + b_l^i), i = 1, \ldots, n.\} \tag{26}
$$

defined as the set of all two-layer neural networks with k hidden neurons equipped with ReLU activation. Then, as long as $k = \Omega(1/h)$, there exists a network in $\mathcal{H}$ for which $Err_{\mathcal{H}} = 0$.

Proof. The proof follows a recent result by Bubeck et al. [46]. Let the output resolution of the network be n. For a fixed p, consider the (linear) vector space spanned by all possible (perhaps uncountably many) basis functions of the form

$$f(\cdot) = a_l^i \text{ReLU}(\langle w_l^i, \cdot \rangle + b_l)$$

where a, b, w are arbitrary real-valued weights. Since $i = 1, \ldots, n$, the span of this space is no more than n-dimensional and isomorphic to $\mathbb{R}^m$ for some $m \leq n$. Therefore, there is a set of no more than n basis functions (i.e., n neurons) that can be used to represent u_p^* any fixed p. Assuming the dimension of p is small, we have $n \lesssim 1/h$. Therefore, $k = \Omega(1/h)$ neurons are sufficient to reproduce u_p^*. ■

Notice that the above theorem shows that there exist NEUFENET architectures that exactly drive the modeling error down to zero. However, the proof is *non-constructive*, and there is no obvious algorithm to find the basis functions that reproduce the solution at the evaluation points. Theorem 5.2 essentially allows us to choose the neural network parameter family Θ such that the modeling error $e_{\mathcal{H}}$ is low. Since, we are free to choose the network architecture, we can always assume (and *a posteriori* confirm) that

$$\|e_{\mathcal{H}}\| = \|u_{\tilde{\theta}} - u^h\| \leq \epsilon, \;\; \epsilon > 0. \tag{27}$$

Remark 3. NEUFENET is designed to be agnostic to a neural network. Therefore, both fully connected neural network as well as convolutional neural networks can be used for the network approximation. Since a convolutional neural network can be interpreted as a special case of a fully connected network with sparse weights [47], the above estimate still holds.

For the third source of error, i.e., the error due to discretization using finite element method can be estimated from standard finite element analysis literature. We start with the following assumption:

Assumption 5.3. *Assume that the spatial domain D is discretized by a mesh $\mathcal{K}^h$ that consists of hyperrectangular elements. Each element $K \in \mathcal{K}^h$ has a bounded radius, i.e., $0 < h_{min} \leq r(K) \leq h_{max} < \infty$. We define the mesh length $h = \min\{r(K)\}_{i=1}^{n_{el}}$*

Lemma 5.4. *The exact solution to Equation 9, $u \in H^2(D)$.*

Proof. In Equation 9, the diffusivity $\nu(\mathbf{x}; \omega) \in C(D)$ for any fixed $\omega \in \Omega$. Furthermore, the forcing function $f = 0 \in L^2(D)$. Using results from regularity theory (such as [26], Sec. 6.3 Theorem 1), we conclude $u \in H^2(D)$. ■

Lemma 5.5. *Let Assumption 5.3 hold. Further assume that the basis functions $\phi_i(\mathbf{x})$ in Equation 14 are chosen such that $\phi_i(\mathbf{x}) \in C^\alpha(K)$ ($\alpha \geq 1$) locally within each element $K \in \mathcal{K}^h$. Then,*

$$\|u^h - u\|_{L^2(D)} \leq C_d h^{\alpha+1}, \tag{28}$$

where $C_d = C_d(D, |u|_{H^2})$ is a constant.

Proof. We refer to standard texts such as Oden and Reddy [48](Sec. 8.6, Theorem 8.5) or Brenner and Scott [21](Sec. 5.7) for the proof. ■

Finally we can write down the estimate for the generalization error in NEUFENET in the form of the following theorem.

Theorem 5.6. *Consider any* NEUFENET *architecture producing fields with grid spacing h. Let $\mathcal{H}$ denote the hypothesis class of all networks obeying that architecture. Suppose that $\Theta \in \mathcal{H}$ is a* NEUFENET *trained using the loss function J defined in Equation 12. Then, its generalization error obeys:*

$$\|e_G\|_{V_\theta} \leq Err_\Theta + Err_{\mathcal{H}} + O(h^{\alpha+1}) \tag{29}$$

where Err_Θ is a term that only depends on the NEUFENET *optimization procedure and $Err_{\mathcal{H}}$ only depends on the choice of hypothesis class $\mathcal{H}$. The α in the third term is the local degree of the basis functions as in Lemma 5.5.*

Proof. The result is simply an application of the triangle inequality. Dropping the subscript V_θ:

$$\begin{aligned}\|e_G\| &= \|u_\theta - u_{\tilde{\theta}} + u_{\tilde{\theta}} - u^h + u^h - u\| \\ &\leq \|u_\theta - u_{\tilde{\theta}}\| + \|u_{\tilde{\theta}} - u^h\| + \|u^h - u\| \\ &= \|e_\theta\| + \|e_{\mathcal{H}}\| + \|e_h\| \\ &= \text{Err}_\Theta + \text{Err}_{\mathcal{H}} + O(h^{\alpha+1})\end{aligned} \tag{30}$$

Using Lemma 5.1, the optimization error Err_Θ is nothing but $\sqrt{2\|\mathcal{E}_J\|_1}$. ■

5.2 Extending the error analysis for the parametric version

The above theorem is for a single parameter choice $p \in \Omega$. An identical argument can be extended to the loss constructed by sampling a *finite* number (say m) of parameters from a distribution over Ω. We obtain the following corollary from Theorem 5.2:

Corollary 1. *Consider a finite-sample version of the loss $\hat{L}_{\text{NEUFENET}}$ constructed by taking the average over m parameter choices sampled from Ω. Consider the hypothesis class:*

$$\mathcal{H} := \{u_\Theta : p \mapsto \sum_{l=1}^{k} a_l^i \mathit{ReLU}(\langle w_l^i, p\rangle + b_l^i), i = 1, \ldots, n.\} \tag{31}$$

defined as the set of all two-layer neural networks with k hidden neurons equipped with ReLU activation. Then, as long as $k = \Omega(m/h)$, there exists a network in $\mathcal{H}$ for which $\mathit{Err}_{\mathcal{H}} = 0$.

This corollary shows that a wide two-layer network exists that can reproduce any (finite) set of field solutions to a PDE system, as long as the width scales linearly in the cardinality of the set. Getting bounds independent of the cardinality is an interesting open question. We have the following result for the optimization error:

Lemma 5.7. *Let u_θ be the solution of the optimization problem in Equation 23 when it is optimized by Algorithm 2. Then the optimization error $\|e_\theta\|_{V_\theta^h} = \sqrt{2\|\mathcal{E}_{\hat{L}}\|_1}$, where $e_\theta = u_\theta - u_{\tilde{\theta}}$, $\mathcal{E}_{\hat{L}} = \hat{L}_{\text{NEUFENET}}(\theta) - \hat{L}_{\text{NEUFENET}}(\tilde{\theta})$.*

Proof. Starting with the definition of $\hat{L}$ from Equation 22 and denoting $\nu_i = \nu(\mathbf{x}, \omega_i)$ and $u_{\theta,i} = u(\mathbf{x}, \omega_i; \theta)$:

$$\hat{L}_{\text{NEUFENET}}(\theta) = \frac{1}{N_s}\sum_{i=1}^{N_s} J(\nu_i, u_{\theta,i}) = \frac{1}{N_s}\sum_{i=1}^{N_s}\left(J(\nu_i, u_{\tilde{\theta},i}) + \frac{1}{2}\|e_{\theta,i}\|_{V^h}^2\right) = \hat{L}_{\text{NEUFENET}}(\tilde{\theta}) + \frac{1}{2}\|e_\theta\|_{V_\theta^h}^2, \tag{32}$$

where we have used $\|e_\theta\|_{V_\theta^h}^2 = \mathbb{E}\|e_\theta\|_{V^h} = \frac{1}{N_s}\sum_{i=1}^{N_s}\|e_{\theta,i}\|_{V^h}^2$. Denoting $\mathcal{E}_{\hat{L}} = \hat{L}_{\text{NEUFENET}}(\theta) - \hat{L}_{\text{NEUFENET}}(\tilde{\theta}) > 0$, we have the result. ■

With this, an analogue of Theorem 5.6 can be stated for the parametric training with finite data as below.

Theorem 5.8. *Consider any* NEUFENET *architecture producing fields with grid spacing h. Let $\mathcal{H}$ denote the hypothesis class of all networks obeying that architecture. Suppose that $\Theta \in \mathcal{H}$ is a* NEUFENET *trained using the loss function $\hat{L}_{\text{NEUFENET}}$ defined in Equation 22. Then, its generalization error obeys:*

$$\|e_G\|_{V_\theta^h} \leq \mathit{Err}_\Theta + \mathit{Err}_{\mathcal{H}} + O(h^{\alpha+1}) \tag{33}$$

where Err_Θ is a term that only depends on the NEUFENET *optimization procedure; $\mathit{Err}_{\mathcal{H}}$ only depends on the choice of hypothesis class $\mathcal{H}$ and α is the local degree of the basis function as in Lemma 5.5.*

Proof. The result is simply an application of the triangle inequality. Dropping the subscript V_θ:

$$\begin{aligned}\|e_G\|_{V_\theta^h} &= \|u_\theta - u_{\tilde{\theta}} + u_{\tilde{\theta}} - u^h + u^h - u\|_{V_\theta^h} \\ &\leq \|u_\theta - u_{\tilde{\theta}}\|_{V_\theta^h} + \|u_{\tilde{\theta}} - u^h\|_{V_\theta^h} + \|u^h - u\|_{V_\theta^h} \\ &\leq \|e_\theta\|_{V_\theta^h} + \|e_{\mathcal{H}}\|_{V_\theta^h} + \|e_h\|_{V_\theta^h}.\end{aligned} \tag{34}$$

The third norm can be estimated as

$$\|e_h\|_{V_\theta^h} = \|u^h - u\|_{V_\theta^h} = \sqrt{\mathbb{E}_{\omega\sim\Omega}\|u_i^h(\omega) - u(\omega)\|_V^2} = \sqrt{\frac{1}{N_s}\sum_{i=1}^{N_s}\|u_i^h - u_i\|_V^2} \leq \sqrt{\frac{1}{N_s}\sum_{i=1}^{N_s}\|\nu_i\|_{L^2(D)}^2\|\nabla(u_i^h - u_i)\|_{L^2(D)}^2}$$
$$\leq \sqrt{\frac{1}{N_s}\sum_{i=1}^{N_s}\|\nu_i\|_{L^2(D)}^2\left(\sum_{K\in\mathcal{K}^h}\|\nabla(u_i^h - u_i)\|_{L^2(K)}^2\right)} \leq \sqrt{\frac{1}{N_s}\sum_{i=1}^{N_s}\|\nu_i\|_{L^2(D)}^2 C_I^h\left(\sum_{K\in\mathcal{K}^h}\|(u_i^h - u_i)\|_{L^2(K)}^2\right)}$$
$$= \sqrt{\frac{1}{N_s}\sum_{i=1}^{N_s}C_I^h\|\nu_i\|_{L^2(D)}^2\|(u_i^h - u_i)\|_{L^2(D)}^2} \leq \sqrt{\frac{1}{N_s}\sum_{i=1}^{N_s}C_{di}h^{2(\alpha+1)}} \leq C_e h^{\alpha+1},$$

where $C_e = C_e\left(\hat{\Omega}_{N_s}, D, C_I^h, A, B\right)$. Here C_I^h is the discrete inverse Poincaré constant such that $\|\nabla u\|_{L^2(K)} \leq C_I^h\|u\|_{L^2(K)}$ for all $K \in \mathcal{K}^h$; $A = \max\{\|\nu_i\|_{L^2(D)}\}_{i=1}^{N_s}$ and $B = \max\{|u_i|_{H^2(D)}\}_{i=1}^{N_s}$. ■

6 Results

6.1 Error convergence for a Poisson problem

At the outset, we would like to validate the error bounds stated in Section 5. To this end, we solve the following non-parametric Poisson's equation:

$$-\Delta u = f \text{ in } D \subset \mathbb{R}^2 \tag{35a}$$
$$u = 0 \text{ on } \partial D, \tag{35b}$$

where $D = [0,1]^2$ is a two-dimensional square domain. The forcing is chosen as

$$f = f(\mathbf{x}) = f(x,y) = 2\pi^2\sin(\pi x)\sin(\pi y). \tag{36}$$

The exact solution to Equation 35 with the forcing function shown in Equation 36 is given by $u_{ex}(x,y) = \sin(\pi x)\sin(\pi y)$. For solving this problem, we seek to train a NEUFENET that can predict the solution u given the forcing f. At the discrete level, the network takes input F^d and outputs U^d. The loss function Equation 11 takes the concrete form:

$$J(u) = \frac{1}{2}\int|\nabla u|^2 d\mathbf{x} - \int u f d\mathbf{x}. \tag{37}$$

Figure 5 shows the contours of the network input F^d, output U^d, the exact solution evaluated on the mesh $\mathcal{K}^h$ (a 256×256 grid) and the error $(U^d - U_{ex})$.

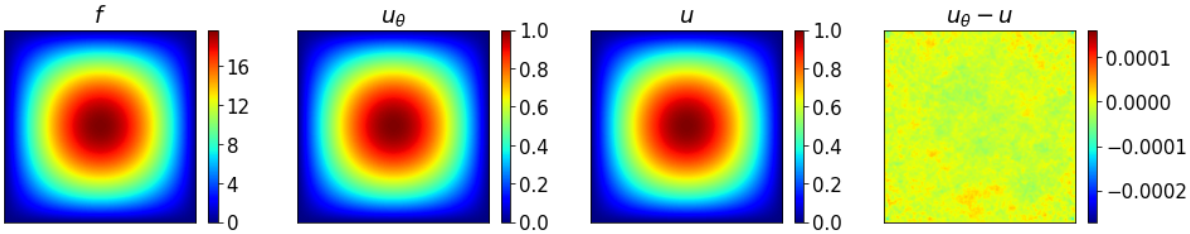


Figure 5: *Solution to Equation 35 with the forcing term as shown in Equation 36 on a* 256×256 *grid. (Left) the discrete forcing* F^d*, (middle-left) the solution* U^d *obtained from a* NEUFENET *with a U-net architecture, (middle-right) the exact solution* $u_{ex} = \sin(\pi x)\sin(\pi y)$ *evaluated on the mesh, denoted* U_{ex}^d*, (right) the error* $(U^d - U_{ex}^d)$*. From left to right:* f*,* u_θ^h*,* u_{num} *and* $(u_\theta^h - u_{num})$*. Note:* $\|u_\theta\| = 0.499979$*,* $\|u\| = 0.5$*,* $\|u_\theta - u\| = 2.4 \times 10^{-5}$*.*

To study convergence behavior, we repeat this procedure with varying mesh length h, starting from $h = \frac{1}{8}$ and gradually decreasing h till $h = \frac{1}{256}$. The calculated errors for each resolution are reported in Figure 6.

Theorem 5.6 estimates the total error by the contributions from three individual sources of errors, namely, the error due to finite element discretization (e_h), the error due to network approximation capacity $(e_{\mathcal{H}})$ and the error due to the

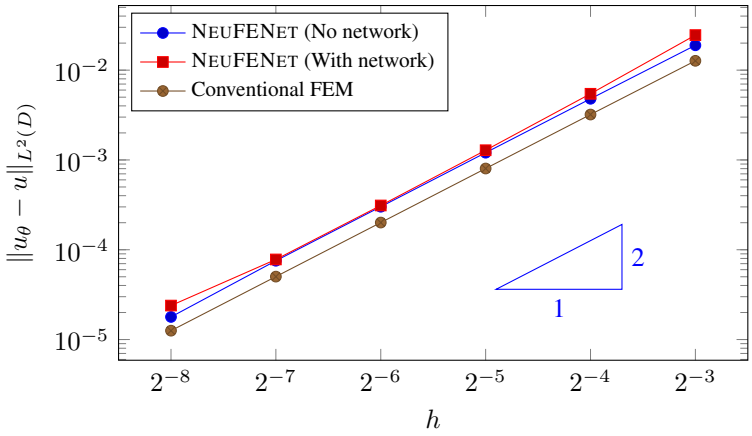


Figure 6: *Convergence of the error in L^2 norm for the Poisson's equation with analytical solution $u = \sin(\pi x)\sin(\pi y)$.*

optimization process (e_θ). Of these three errors, e_h maintains a particular relation to the discretization parameter h (i.e., the mesh size). The other two errors do not hold a straight-forward relation with the mesh size or the network parameters. Thus, we put the estimate in Equation 29 to test by keeping both $e_{\mathcal{H}}$ and e_θ sufficiently low, so that the dominating error is the discretization error e_h.

We illustrate this by running two sets of NeuFENet simulations.

- The first set is where we completely remove the neural network and optimize the loss directly with respect to the function u^h, i.e.,

$$u^h = \underset{u^h \in V^h}{\arg\min}\, J(u^h), \tag{38}$$

  which is nothing but a classic Rayleigh-Ritz optimization. The absence of a neural network eliminates the error $e_{\mathcal{H}}$. So the total error is a combination of only e_h and e_θ. The total errors from this algorithm are plotted against the mesh size h in Figure 6 under the legend "NeuFENet (No network)". We see that the error plot has a slope of 2.

- The second set uses a neural network. Thus the optimization statement is the same as presented in Equation 18. Therefore, as discussed in Theorem 5.6, the total error is a combination of all three errors indicated in Equation 29. To keep $e_{\mathcal{H}}$ negligible, we need to be cognizant of the fact that the spatial degrees of freedom (i.e., the number of bases in V^h) is inversely proportional to h^2 (for a 2D domain). Thus, as we decrease h, the "size" of V^h increases. Therefore the function space V_θ^h must also get bigger, in particular, it should be big enough to satisfy $V_\theta^h \supset V^h$. One way to accommodate this fact is to use a high-capacity network to solve the equation at all h-levels. But the UNet architecture described in Section 4.1 does not allow very high depth when the input/output size is low. Thus, we must enhance the network capacity at different h levels gradually by increasing the network depth. Using this strategy, we solve Equation 35 at various h-levels and plot the errors in Figure 6. The slope of 2 of the error curve once again confirms that both $e_{\mathcal{H}} \approx 0$ and $e_\theta \approx 0$. Interestingly, if we do not keep $e_{\mathcal{H}}$ negligible by increasing the depth of the network for smaller h, both $e_{\mathcal{H}}$ and e_θ can dominate (see B). This suggests that gradual increase in network complexity is warranted as the discretization becomes finer. This is made computationally efficient by using multi-grid like approaches [49].

Figure 6 also shows a plot of errors obtained from solving the same problem using a conventional FEM code (using numerical linear algebra) for reference. We use a GMRES solver with a tolerance of 10^{-8}.

6.2 Poisson's equation with parametric log permeability

Our second illustration is the solution of the PDE defined in Section 2.1 (Equation 5), which is frequently used for simulating practical problems such as heat or mass transfer through an inhomogeneous media. We solve this problem in both 2D and 3D domains, i.e., $D = [0,1]^2$ as well as $D = [0,1]^3$; $\tilde{\nu}$ is now a function of $\mathbf{x} = (x, y)$ and is also parametric, as mentioned in Equation 47.

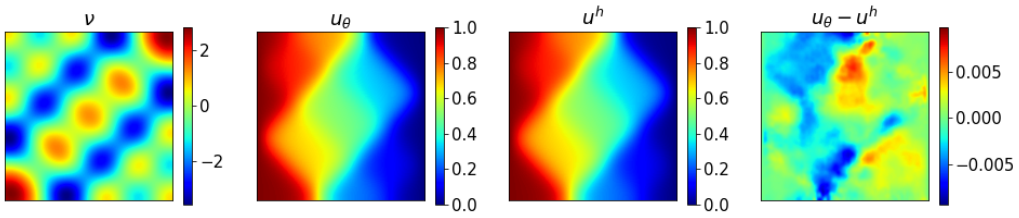


Figure 7: *(Left) contours of* $\ln(\nu)$ *corresponding to* $\underline{a} = (-0.24, -0.17, 0.13, 0.07, -0.07, 0.14)$*, (middle-left)* NEUFENET *prediction* (u_θ)*, (midddle-right) reference numerical solution using FEM* (u^h)*, (right) contours of* $(u_\theta - u^h)$

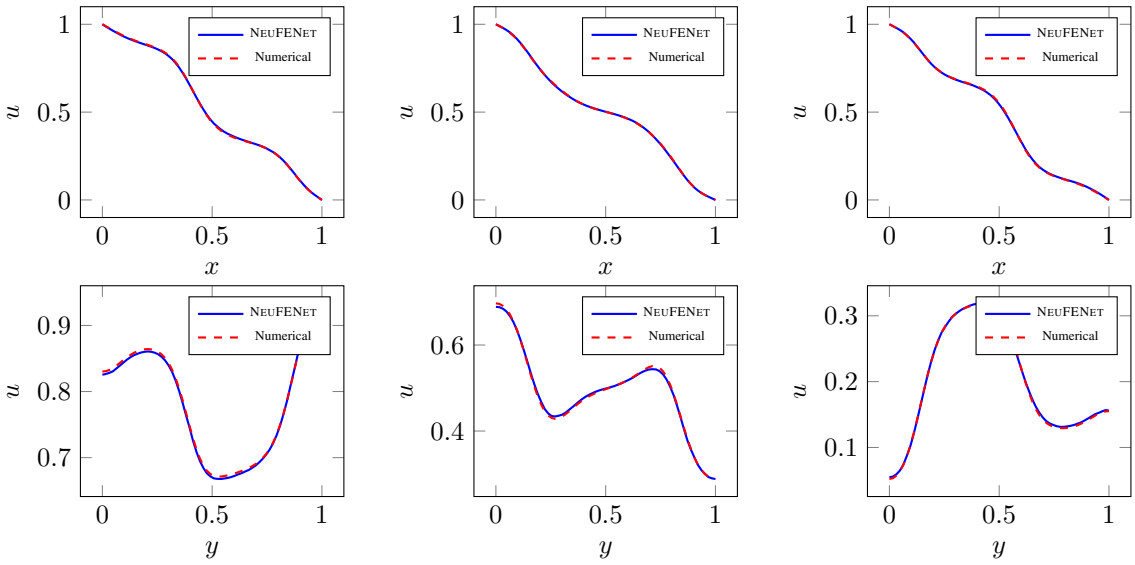


Figure 8: *Line cuts for the contours presented in Fig 7. (Top row)* x*-parallel line cuts at* $y = 0.2, 0.5, 0.8$*. (Bottom row)* y*-parallel line cuts at* $x = 0.2, 0.5, 0.8$*.*

We seek a mapping of the form $u = G_{nn}(\nu)$, where G_{nn} denotes the neural network. So S^d refers to the discrete version of ν. Following the principle of Karhunen-Loeve expansion as described in A, the infinite dimensional random space is truncated into a finite dimensional space. Thereafter, a finite set of samples are prepared from this space for the training process. Suppose the number of samples is N_s. Then the loss function takes the concrete form:

$$J = \frac{1}{N_s} \sum_{i=1}^{N_s} \int_D \tilde{\nu}_i(\mathbf{x}) |\nabla u_i(\mathbf{x})|^2 d\mathbf{x}, \tag{39}$$

where, $u_i = G_{nn}(\nu_i, \theta)$. Both Dirichlet and Neumann conditions are present in this equation. In NEUFENET, the Dirichlet conditions are applied exactly. The zero-Neumann condition is also applied exactly at the continuous level, since the boundary integrals vanish at the continuous level (see Equation 10).

By optimizing the loss (Equation 39), we attempt to learn the distribution of the stochastic solution, given that the coefficients in the log permeability K-L sum come from a known range of values that depends on the parameter space ω. We truncate the K-L sum after 6 terms. These six coefficients form a six-dimensional space from which the coefficient tuples $\{a_i\}_{i=1}^6$ can be drawn. The NEUFENET is trained by selecting a finite number (N_s) of pseudo-random samples from this 6-dimensional space, specifically $\mathbf{a} \in [-\sqrt{3}, \sqrt{3}]^6$ (see also A). For the results shown below, we have taken $N_s = 65536$. We used the Adam optimization algorithm, with a learning rate of 10^{-4}. Once the network is trained, ***we can perform inference by evaluating the solution for any diffusivity*** ν ***taken from the sample space***. To illustrate the nature of the input (ν or S^d) and the solution (u or U^d), we present an anecdotal (i.e., a non-special and random) set of S^d and U^d in Figure 7. A reference solution using a conventional FEM program is also presented therein. Furthermore, sectional line cuts for these contours are shown in Figure 8. The line cuts display a close match between NEUFENET and the numerical solution.

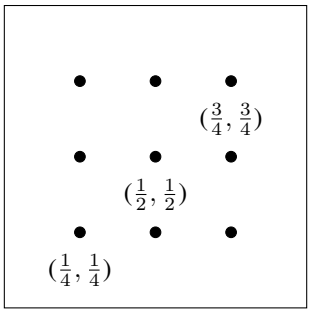


Figure 9: *Query points for histogram analysis. Positions of points denoted by (x, y) tuple.*

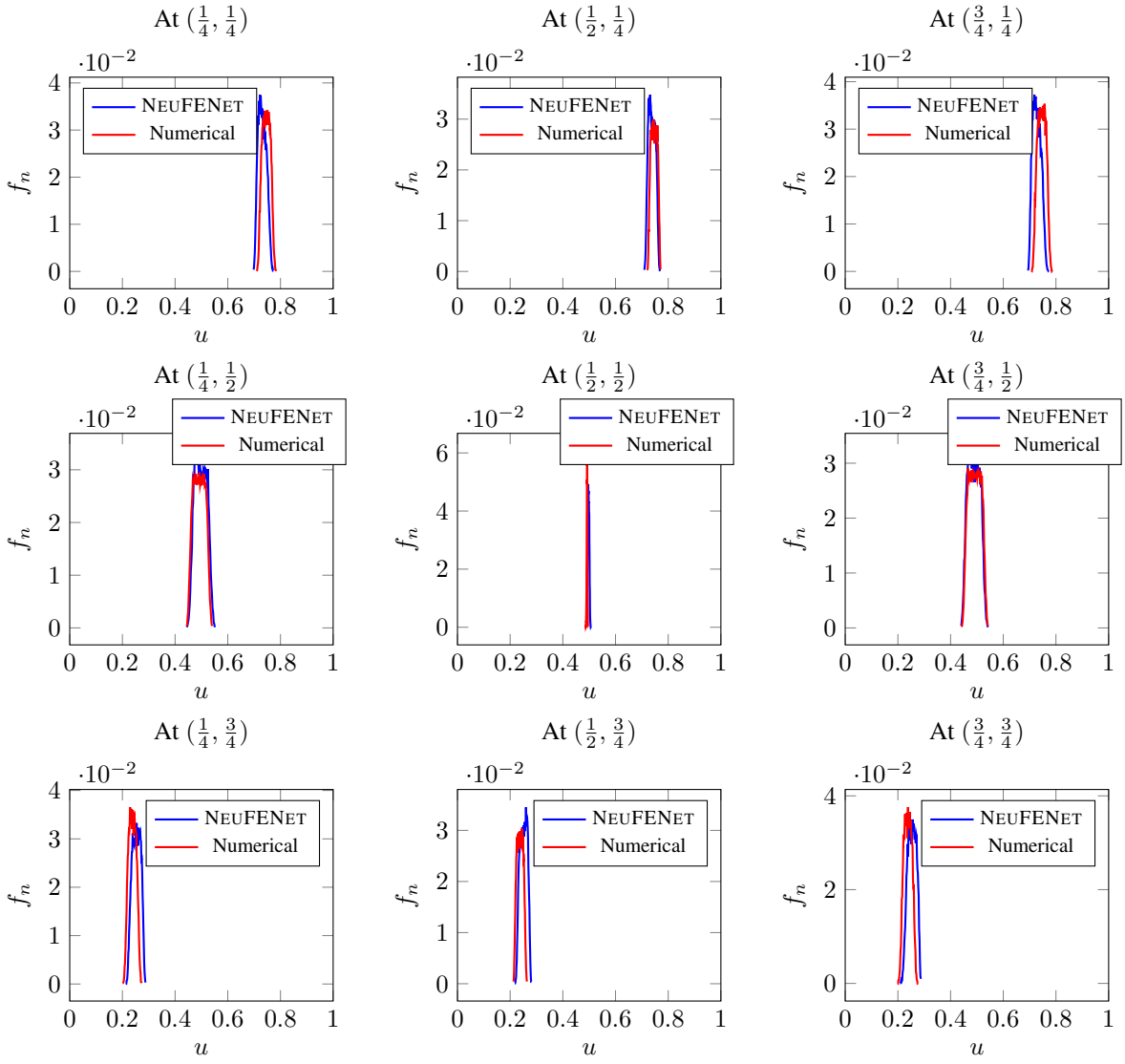


Figure 10: *Normalized histograms plotted for the query points shown in Figure 9.*

6.2.1 Statistical distribution of solution

Since Equation 5 is parametric, we can compare the quality of solution from NeuFENet with a reference numerical solution in a statistical manner. We choose some points on the domain D (shown by black dots in Figure 9) and evaluate

the solution values at those query points for $16,384$ samples of ν, where the $\{a_i\}_{i=1}^6$ tuples are taken from a smaller subset of the full sample space, namely, $\mathbf{a} \in [-\frac{1}{4}, \frac{1}{4}]^6$. Therefore , at a particular query point, those $16,384$ solution values approximately represent a distribution of the solution values at that point. This sample of solution values at each of those query points then allow us to create histograms of the solution values at each query point.

The histograms are shown in Figure 10. We notice a very close match between the histograms obtained from NEUFENET and a conventional FEM solver. This once again confirms that NEUFENET is effective in providing the correct statistics of the parametric Poisson equation.

6.3 3-D Poisson's equation

So far, we have focused on two-dimensional problems. Although 2D problems are useful in demonstrating the key features and properties of NEUFENET method, a real test of neural PDE solvers lies in their ability to solve three-dimensional problems. NEUFENET can solve both 2D and 3D problems without much changes to the architecture. To provide an example of this, we solve the 3D counterpart of the PDE defined in Equation 5, which is:

$$-\nabla \cdot (\tilde{\nu}(\mathbf{x})\nabla u) = 0 \text{ in } D = [0,1]^3, \tag{40a}$$

$$u(x=0,y,z) = 1, \tag{40b}$$

$$u(x=1,y,z) = 0, \tag{40c}$$

$$\hat{\mathbf{n}} \cdot \nabla u = 0 \quad \text{on all other boundaries}, \tag{40d}$$

where $\hat{\mathbf{n}}$ denotes the outward normal to the boundary. Once again, the functional form of $\tilde{\nu(\mathbf{x})}$ is described in A. The loss function is a direct analogue of Equation 39:

$$J = \int_D \tilde{\nu}(\mathbf{x}) |\nabla u(\mathbf{x})|^2 d\mathbf{x}, \tag{41}$$

In Figure 11, we show one randomly selected pair of ν and u for a 3D problem obtained using NEUFENET. We optimize Equation 41 for a randomly selected set of coefficients $\mathbf{a} = (-1, 1.4, 1.5, -1.3, -1.6, 0.3)$. The plots of $\nu(x,y,z)$ and $u_\theta(x,y,z)$ are shown in Figure 11.

7 Conclusions and future directions

In this paper we develop a neural method NEUFENET for solving parametric PDEs where the discretization and the loss functions are inspired by the continuous Galerkin (cG) method and the Rayleigh-Ritz method respectively. Due to the choice of discretization scheme, NEUFENET inherits the approximation properties of the cG method. This allows us to: (i) calculate spatial derivatives in the same way as in finite element methods, (ii) perform spatial integration using simple Gaussian quadrature schemes, (iii) apply Dirichlet and (zero) Neumann boundary conditions exactly and (iv) derive *a priori* error estimates.

The optimization problem is defined in terms of an energy functional derived from variational principles. This is in contrast to residual based minimization which is the more widely followed process across the current neural methods, albeit with exceptions (such as Yu et al. [28]). We showed examples of Poisson's equation solved using NEUFENET. Since Poisson's equation is a self-adjoint equation, its energy functional is convex and thus possesses a unique minima, which can be easily found by a gradient based optimization method. We further illustrate that such a method can successfully be used to solve stochastic PDEs and determine its statistical properties.

We identify some disadvantages and opportunities for future work. NEUFENET as described in this paper suits "steady-state" equations such as the Poisson's equation or other similar equations. We hypothesize that NEUFENET may require additional features for solving parabolic equations because the full space-time functional is not convex. Since NEUFENET uses discretization provided by a finite element method, therefore NEUFENET is mesh based. It must be noted that for the examples shown in this paper, we did not need to store a mesh explicitly because the meshes were structured meshes and fully regular. But for an arbitrary geometry, such a mesh will need to be saved to memory. Because of the requirement of mesh in NEUFENET, it can be memory-intensive, especially for 3D or higher dimensional problems. But this issue can be alleviated by considering distributed frameworks (such as Balu et al. [49]). We anticipate that such approaches that tightly integrate neural architectures with well developed scientific computing approaches will prove successful towards our goal of a (near) real time neural PDE inference.

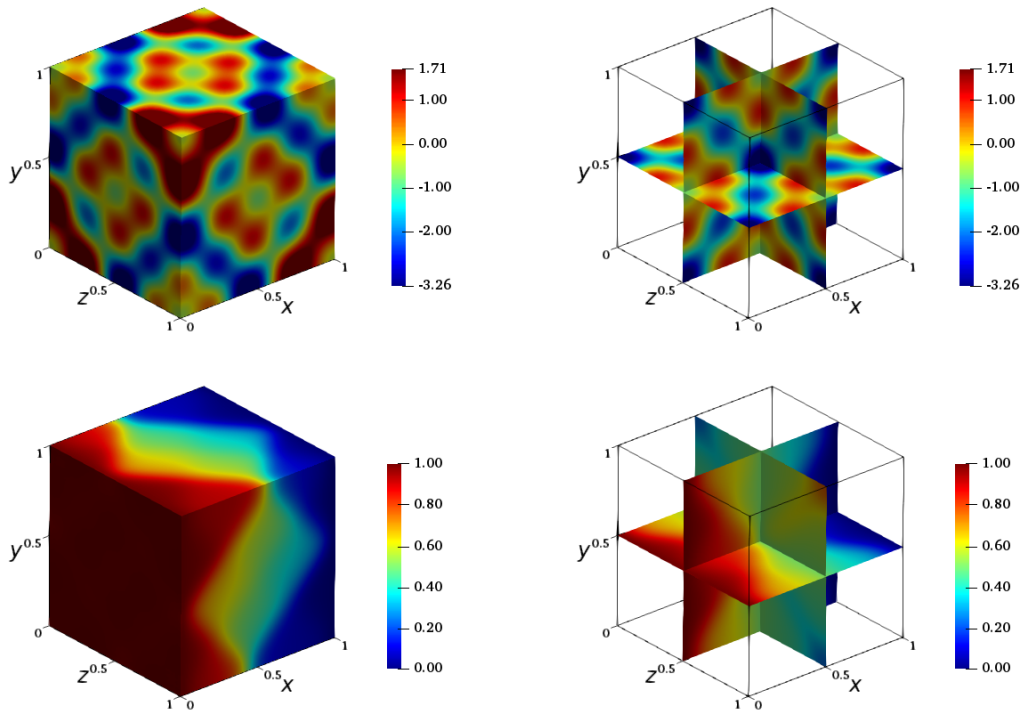


Figure 11: *Contours of* $\ln(\nu(x, y, z))$ *and the solution* $u_\theta(x, y, z)$ *to the 3D Poisson's problem (Equation 40) on a* $64 \times 64 \times 64$ *mesh (for* $\mathbf{a} = (-1, 1.4, 1.5, -1.3, -1.6, 0.3)$*).*

Acknowledgements

This work was supported in part by the National Science Foundation under grants CCF-2005804, LEAP-HI-2053760, CMMI-1644441, CPS-FRONTIER-1954556, USDA-NIFA-2021-67021-35329 and ARPA-E DIFFERENTIATE-DE-AR0001215. Any information provided and opinions expressed in this material are those of the author(s) and do not necessarily reflect the views of, nor any endorsements by, the funding agencies.

References

[1] Raissi, M, Perdikaris, P, Karniadakis, GE. Physics-informed neural networks: A deep learning framework for solving forward and inverse problems involving nonlinear partial differential equations. Journal of Computational Physics 2019;378:686–707.

[2] Rudy, S, Alla, A, Brunton, SL, Kutz, JN. Data-driven identification of parametric partial differential equations. SIAM Journal on Applied Dynamical Systems 2019;18(2):643–660.

[3] Tompson, J, Schlachter, K, Sprechmann, P, Perlin, K. Accelerating eulerian fluid simulation with convolutional networks. In: International Conference on Machine Learning. PMLR; 2017, p. 3424–3433.

[4] Raissi, M, Karniadakis, GE. Hidden physics models: Machine learning of nonlinear partial differential equations. Journal of Computational Physics 2018;357:125–141.

[5] Lu, L, Jin, P, Karniadakis, GE. Deeponet: Learning nonlinear operators for identifying differential equations based on the universal approximation theorem of operators. arXiv preprint arXiv:191003193 2019;.

[6] Kharazmi, E, Zhang, Z, Karniadakis, GE. Variational physics-informed neural networks for solving partial differential equations. arXiv preprint arXiv:191200873 2019;.

[7] Sirignano, J, Spiliopoulos, K. Dgm: A deep learning algorithm for solving partial differential equations. Journal of computational physics 2018;375:1339–1364.

[8] Yang, L, Zhang, D, Karniadakis, GE. Physics-informed generative adversarial networks for stochastic differential equations. arXiv preprint arXiv:181102033 2018;.

[9] Pang, G, Lu, L, Karniadakis, GE. fpinns: Fractional physics-informed neural networks. SIAM Journal on Scientific Computing 2019;41(4):A2603–A2626.

[10] Karumuri, S, Tripathy, R, Bilionis, I, Panchal, J. Simulator-free solution of high-dimensional stochastic elliptic partial differential equations using deep neural networks. Journal of Computational Physics 2020;404:109120.

[11] Han, J, Jentzen, A, Weinan, E. Solving high-dimensional partial differential equations using deep learning. Proceedings of the National Academy of Sciences 2018;115(34):8505–8510.

[12] Michoski, C, Milosavljevic, M, Oliver, T, Hatch, D. Solving irregular and data-enriched differential equations using deep neural networks. arXiv preprint arXiv:190504351 2019;.

[13] Samaniego, E, Anitescu, C, Goswami, S, Nguyen-Thanh, VM, Guo, H, Hamdia, K, et al. An energy approach to the solution of partial differential equations in computational mechanics via machine learning: Concepts, implementation and applications. Computer Methods in Applied Mechanics and Engineering 2020;362:112790.

[14] Ramabathiran, AA, Ramachandran, P. Spinn: Sparse, physics-based, and partially interpretable neural networks for pdes. Journal of Computational Physics 2021;445:110600.

[15] Botelho, S, Joshi, A, Khara, B, Sarkar, S, Hegde, C, Adavani, S, et al. Deep generative models that solve pdes: Distributed computing for training large data-free models. arXiv preprint arXiv:200712792 2020;.

[16] Sitzmann, V, Martel, J, Bergman, A, Lindell, D, Wetzstein, G. Implicit neural representations with periodic activation functions. Advances in Neural Information Processing Systems 2020;33.

[17] Mishra, S, Rusch, TK. Enhancing accuracy of deep learning algorithms by training with low-discrepancy sequences. SIAM Journal on Numerical Analysis 2021;59(3):1811–1834.

[18] Zhu, Y, Zabaras, N, Koutsourelakis, PS, Perdikaris, P. Physics-constrained deep learning for high-dimensional surrogate modeling and uncertainty quantification without labeled data. Journal of Computational Physics 2019;394:56–81.

[19] Wen, G, Li, Z, Azizzadenesheli, K, Anandkumar, A, Benson, SM. U-fno–an enhanced fourier neural operator based-deep learning model for multiphase flow. arXiv preprint arXiv:210903697 2021;.

[20] Ranade, R, Hill, C, Pathak, J. Discretizationnet: A machine-learning based solver for navier–stokes equations using finite volume discretization. Computer Methods in Applied Mechanics and Engineering 2021;378:113722.

[21] Brenner, S, Scott, R. The mathematical theory of finite element methods; vol. 15. Springer Science & Business Media; 2007.

[22] Larson, MG, Bengzon, F. The finite element method: theory, implementation, and applications; vol. 10. Springer Science & Business Media; 2013.

[23] Shin, Y, Zhang, Z, Karniadakis, GE. Error estimates of residual minimization using neural networks for linear pdes. arXiv preprint arXiv:201008019 2020;.

[24] Mishra, S, Molinaro, R. Estimates on the generalization error of physics informed neural networks (pinns) for approximating pdes. arXiv preprint arXiv:200616144 2020;.

[25] Jiao, Y, Lai, Y, Luo, Y, Wang, Y, Yang, Y. Error analysis of deep ritz methods for elliptic equations. arXiv preprint arXiv:210714478 2021;.

[26] Evans, LC. Partial differential equations. Graduate studies in mathematics 1998;19(4):7.

[27] Reddy, J. An introduction to the finite element method; vol. 1221. McGraw-Hill New York; 2010.

[28] Yu, B, et al. The deep ritz method: a deep learning-based numerical algorithm for solving variational problems. arXiv preprint arXiv:171000211 2017;.

[29] Lee, H, Kang, IS. Neural algorithm for solving differential equations. Journal of Computational Physics 1990;91(1):110–131.

[30] Lagaris, IE, Likas, A, Fotiadis, DI. Artificial neural networks for solving ordinary and partial differential equations. IEEE transactions on neural networks 1998;9(5):987–1000.

[31] Malek, A, Beidokhti, RS. Numerical solution for high order differential equations using a hybrid neural network optimization method. Applied Mathematics and Computation 2006;183(1):260–271.

[32] Sukumar, N, Srivastava, A. Exact imposition of boundary conditions with distance functions in physics-informed deep neural networks. arXiv preprint arXiv:210408426 2021;.

[33] Lagaris, IE, Likas, AC, Papageorgiou, DG. Neural-network methods for boundary value problems with irregular boundaries. IEEE Transactions on Neural Networks 2000;11(5):1041–1049.

[34] Van der Meer, R, Oosterlee, C, Borovykh, A. Optimally weighted loss functions for solving pdes with neural networks. arXiv preprint arXiv:200206269 2020;.

[35] Wang, S, Teng, Y, Perdikaris, P. Understanding and mitigating gradient pathologies in physics-informed neural networks. arXiv preprint arXiv:200104536 2020;.

[36] Hennigh, O, Narasimhan, S, Nabian, MA, Subramaniam, A, Tangsali, K, Fang, Z, et al. Nvidia simnet: An ai-accelerated multi-physics simulation framework. In: International Conference on Computational Science. Springer; 2021, p. 447–461.

[37] Wang, S, Perdikaris, P. Long-time integration of parametric evolution equations with physics-informed deeponets. arXiv preprint arXiv:210605384 2021;.

[38] Paganini, M, de Oliveira, L, Nachman, B. Calogan: Simulating 3d high energy particle showers in multilayer electromagnetic calorimeters with generative adversarial networks. Physical Review D 2018;97(1):014021.

[39] Krishnapriyan, AS, Gholami, A, Zhe, S, Kirby, RM, Mahoney, MW. Characterizing possible failure modes in physics-informed neural networks. arXiv preprint arXiv:210901050 2021;.

[40] Wang, S, Teng, Y, Perdikaris, P. Understanding and mitigating gradient flow pathologies in physics-informed neural networks. SIAM Journal on Scientific Computing 2021;43(5):A3055–A3081.

[41] Fox, C. An introduction to the calculus of variations. Courier Corporation; 1987.

[42] Kingma, DP, Ba, J. Adam: A method for stochastic optimization. arXiv preprint arXiv:14126980 2014;.

[43] Ronneberger, O, Fischer, P, Brox, T. U-net: Convolutional networks for biomedical image segmentation. In: International Conference on Medical image computing and computer-assisted intervention. Springer; 2015, p. 234–241.

[44] Çiçek, Ö, Abdulkadir, A, Lienkamp, SS, Brox, T, Ronneberger, O. 3D U-Net: learning dense volumetric segmentation from sparse annotation. In: International conference on medical image computing and computer-assisted intervention. Springer; 2016, p. 424–432.

[45] Paszke, A, Gross, S, Massa, F, Lerer, A, Bradbury, J, Chanan, G, et al. Pytorch: An imperative style, high-performance deep learning library. Advances in neural information processing systems 2019;32:8026–8037.

[46] Bubeck, S, Eldan, R, Lee, YT, Mikulincer, D. Network size and weights size for memorization with two-layers neural networks. arXiv preprint arXiv:200602855 2020;.

[47] LeCun, Y, Bottou, L, Bengio, Y, Haffner, P. Gradient-based learning applied to document recognition. Proceedings of the IEEE 1998;86(11):2278–2324.

[48] Oden, JT, Reddy, JN. An introduction to the mathematical theory of finite elements. Courier Corporation; 2012.

[49] Balu, A, Botelho, S, Khara, B, Rao, V, Hegde, C, Sarkar, S, et al. Distributed multigrid neural solvers on megavoxel domains. arXiv preprint arXiv:210414538 2021;.

[50] Ghanem, RG, Spanos, PD. Stochastic finite elements: a spectral approach. Courier Corporation; 2003.

A Representation of random diffusivity

With ω taken from the sample space Ω, the diffusivity / permeability ν can be written as an exponential of a random quantity Z:

$$\nu = \exp\left(Z(\mathbf{x};\omega)\right). \tag{42}$$

We assume that Z is square integrable, i.e., $\mathbb{E}\left[|Z(\mathbf{x};\omega)|^2\right] < \infty$. Then we can write Z using the Karhunen-Loeve expansion [50], as:

$$Z(\mathbf{x};\omega) = \bar{Z}(\mathbf{x}) + \sum_{i=1}^{\infty} \sqrt{\lambda_i}\phi_i(\mathbf{x})\psi_i(\omega), \tag{43}$$

where $\bar{Z}(\mathbf{x}) = \mathbb{E}(Z(\mathbf{x},\omega))$, and $\psi_i(\omega)$ are independent random variables with zero mean and unit variance. λ_i and $\phi_i(\mathbf{x})$ are the eigenvalues and eigenvectors corresponding to the Fredholm equation:

$$\int_D C_Z(\mathbf{s},\mathbf{t})\phi(s)ds = \lambda\phi(\mathbf{t}), \tag{44}$$

where $C_Z(s,t)$ is the covariance kernel given by,

$$C_Z(\mathbf{s},\mathbf{t}) = \sigma_z^2 \exp\left(-\left[\frac{s_1-t_1}{\eta_1} + \frac{s_2-t_2}{\eta_2} + \frac{s_3-t_3}{\eta_3}\right]\right), \tag{45}$$

where η_i is the correlation length in the x_i coordinate. This particular form of the covariance kernel is separable in the three coordinates, thus the eigenvalues and the eigenfunctions of the multi-dimensional case can be obtained by combining the eigenvalues and eigenfunctions of the one-dimensional covariance kernel given by:

$$C_Z(s,t) = \sigma_Z^2 \exp\left(-\frac{s-t}{\eta}\right), \tag{46}$$

where σ_Z is the variance and η is the correlation length in one-dimension.

Equation 42 can then be written as,

$$\tilde{\nu}(\mathbf{x};\omega) = \exp\left(\sum_{i=1}^{m} a_i \sqrt{\lambda_{xi}\lambda_{yi}}\phi_i(x)\psi_i(y)\right) \tag{47}$$

where a_i is an m-dimensional parameter, λ_x and λ_y are vectors of real numbers arranged in the order of monotonically decreasing values; and ϕ and ψ are functions of x and y respectively. λ_{xi} is calculated as:

$$\lambda_{xi} = \frac{2\eta\sigma_x}{(1+\eta^2\omega_x^2)}, \tag{48}$$

where ω_x is the solution to the system of transcendental equations obtained after differentiating Equation 44 with respect to $\mathbf{t}$. λ_{yi} are calculated similarly. $\phi_i(x)$ are given by:

$$\phi_i(x) = \frac{a_i}{2}\cos(a_i x) + \sin(a_i x) \tag{49}$$

and $\psi_i(y)$ are calculated similarly. We take $m = 6$ and assume that each a_i is uniformly distributed in $[-\sqrt{3},\sqrt{3}]$, thus $\mathbf{a} \in [-\sqrt{3},\sqrt{3}]^6$. The input diffusivity ν in all the examples in Sections 6.2 and 6.3 are calculate by choosing the 6-dimensional coefficient $\mathbf{a}$ from $[-\sqrt{3},\sqrt{3}]^6$.

B Further discussion on convergence studies

B.1 Discussion on the role of keeping $e_{\mathcal{H}}$ and e_θ low

If we choose a fixed network architecture and use it to solve Equation 35 across different h-levels, then the errors do not necessarily decrease with decreasing h. As shown in Figure 12, the errors actually increase when $h > 2^{-5}$. This reason for this behaviour is that, when h becomes low, the number of discrete unknowns in the mesh (i.e., U_i's in Equation 14) increases. In fact, in this case, the number of basis functions / unknowns, N is exactly equal to $\frac{1}{h^2}$. As h decreases, the size of the space V^h increases. But since the network remains the same, the discrete function space V^h does not remain a subspace of V_θ^h anymore. This network function class also needs to get bigger to accommodate all the possible functions at the lower values of h. Figure 12 also shows the errors obtained when the network is indeed enhanced to make $V_\theta^h \supset V$ (this is a clone of the errors plotted in Figure 6).

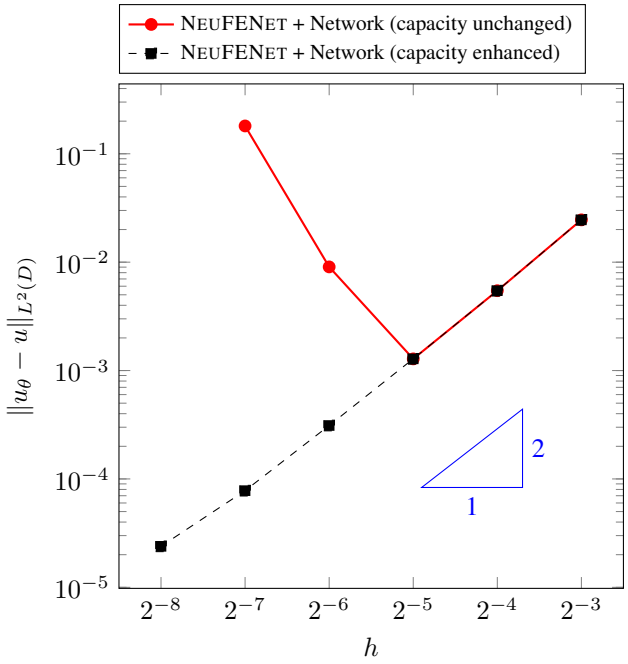


Figure 12: *Convergence of the error in L^2 norm for the Poissson equation with analytical solution $u = \sin(\pi x)\sin(\pi y)$.*

C Solutions to the parametric Poisson's equation

C.1 Randomly selected examples

#	a_1	a_2	a_3	a_4	a_5	a_6	$\|u_\theta\|_{L^2(D)}$	$\|u^h\|_{L^2(D)}$	$\|u_\theta - u^h\|_{L^2(D)}$	$\frac{\|u_\theta - u^h\|_{L^2(D)}}{\|u^h\|_{L^2(D)}}$
1	0.223	0.134	-0.141	-0.215	0.124	-0.201	37.397	37.377	0.150	0.0040
2	0.002	-0.050	0.014	0.183	0.147	-0.096	38.673	38.657	0.269	0.0069
3	0.182	-0.246	-0.087	-0.132	0.024	-0.052	37.446	37.464	0.237	0.0063
4	0.143	0.048	0.098	-0.090	-0.101	-0.071	37.929	37.972	0.234	0.0062
5	-0.133	-0.020	-0.110	0.194	0.093	0.022	37.912	37.825	0.253	0.0067

Table 1: *Norm of solution fields for a few randomly selected*

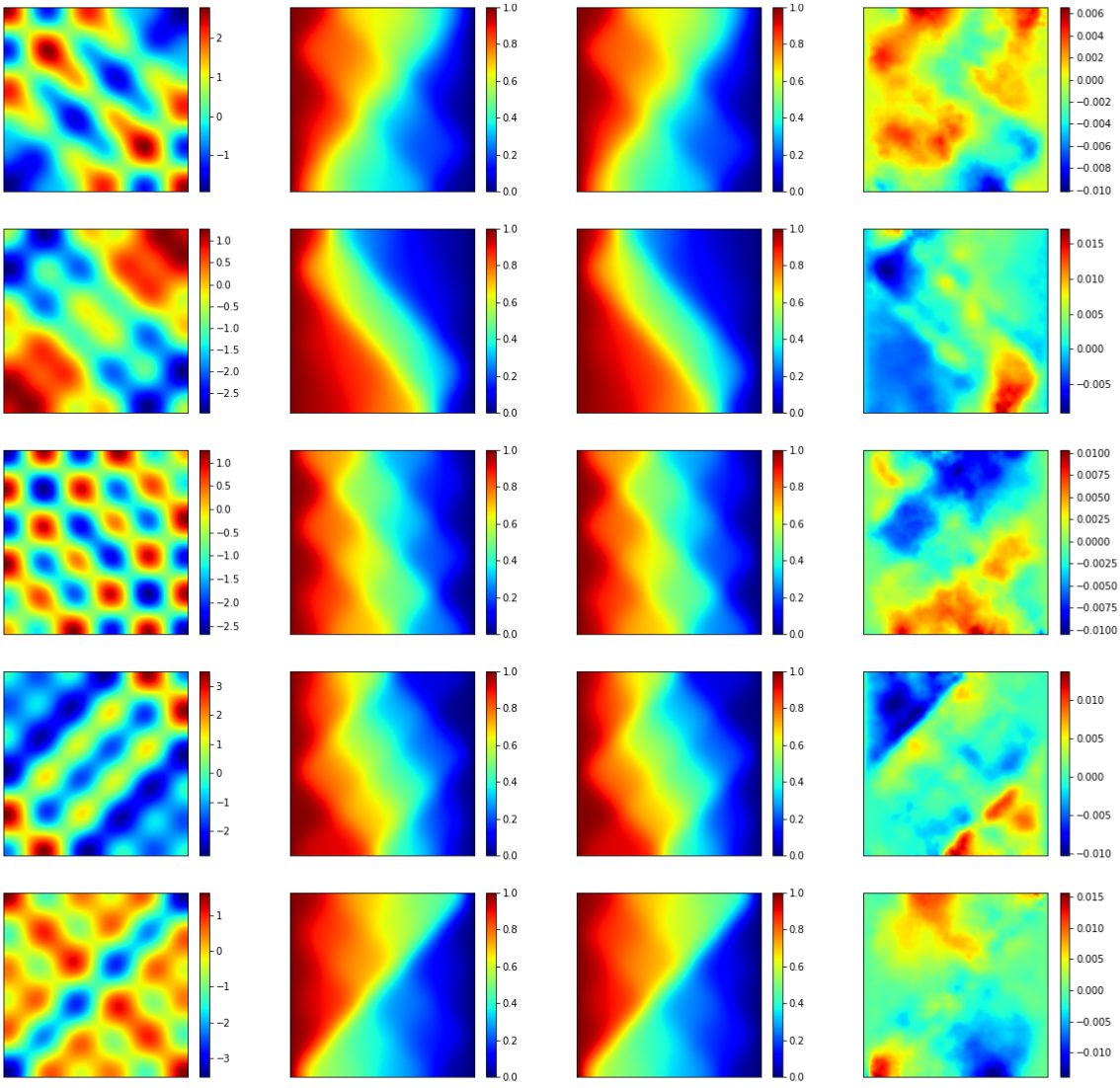


Figure 13: *Contours for the randomly selected examples presented in Table 1: (left)* $\ln(\nu)$*, (mid-left)* u_θ*, (mid-right)* u^h *and (right)* $(u_\theta - u^h)$

C.2 Mean and standard-deviation fields

	$\|u_\theta\|_{L^2(D)}$	$\|u^h\|_{L^2(D)}$	$\|u_\theta - u^h\|_{L^2(D)}$	$\frac{\|u_\theta - u^h\|_{L^2(D)}}{\|u^h\|_{L^2(D)}}$
Mean	36.8186	37.1009	0.7919	0.0214
Std-dev	1.0933	1.0316	0.1407	0.1364

Table 2: *Norm of the mean and standard-deviation fields*

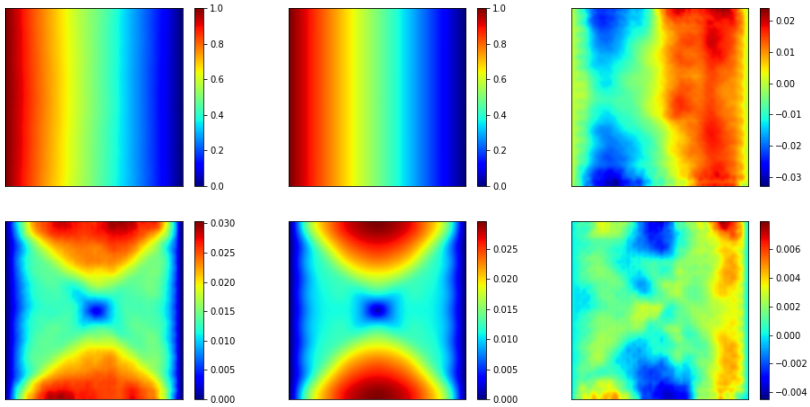


Figure 14: *(top) Mean and (bottom) standard deviation fields: (left)* NEUFENET *(u_θ), (mid) Conventional FEM (u^h, (right) point-wise difference ($u_\theta - u^h$)*